

# High resolution quantum enhanced phase imaging of cells

Alberto Paniate,<sup>1</sup> Giuseppe Ortolano,<sup>1,2,3</sup> Sarika Soman,<sup>4</sup> Marco Genovese,<sup>1</sup> and Ivano Ruo Berchera<sup>1,\*</sup>

<sup>1</sup>*Quantum metrology and nano technologies division,  
INRiM, Strada delle Cacce 91, 10153 Torino, Italy*

<sup>2</sup>*Dipartimento di Fisica e Astronomia, Università di Firenze,  
Via G. Sansone 1, I-50019 Sesto Fiorentino (FI), Italy*

<sup>3</sup>*Istituto Nazionale di Fisica Nucleare, Sezione di Firenze,  
Via G. Sansone 1, I-50019 Sesto Fiorentino (FI), Italy*

<sup>4</sup>*Imaging Physics Dept. Optics Research Group, Faculty of Applied Sciences,  
Delft University of Technology, Lorentzweg 1, 2628CJ Delft, The Netherlands*

Recovering both amplitude and phase information from a system is a fundamental goal of optical imaging. At the same time, it is crucial to use a low photon dose to avoid altering the system, particularly when dealing with biological samples. Quantum imaging offers a powerful approach for extracting more information per photon than classical techniques, which are ultimately limited by shot-noise. However, the trade-off between quantum noise reduction and spatial resolution has been considered a major drawback to the application of quantum techniques to small cellular and sub-cellular structures, where they could offer the most significant benefits. In this work, we overcome this limitation by demonstrating a resolution-independent quantum advantage. We achieve high-resolution phase imaging limited only by the numerical aperture, while simultaneously attaining quantum noise reduction. This enables, for the first time, sub-shot-noise quantitative phase imaging of biological cells. Unlike other quantum imaging approaches, our method operates in a quasi-single-shot wide-field mode, retrieves both phase and amplitude information, and does not rely on interferometric measurements, making it intrinsically fast and stable. These results pave the way for the immediate application of sub-shot-noise imaging in biology.

PACS numbers:

## INTRODUCTION

In biological imaging, many specimens, such as live cells and tissues, are nearly transparent under conventional light microscopy, which makes high-contrast imaging challenging without artificial labeling. Quantitative phase imaging (QPI) addresses this limitation by measuring optical path length differences, providing intrinsic contrast based on sample thickness and refractive index variations [1].

In general, extracting meaningful information from both the amplitude and phase of an object depends critically on two key figures of merit: resolution and sensitivity. Resolution defines the smallest distinguishable details in an image and is influenced by factors such as the optical system, the wavelength of light, and detector properties. Sensitivity, on the other hand, refers to the ability to detect weak signals, which is crucial for imaging faint biological structures. Sensitivity is often limited by photon quantum noise (shot-noise) and becomes a bottleneck when increasing the illumination level, which may induce phototoxicity or interfere with the biological processes under study. Often, improving resolution may be detrimental to sensitivity and vice versa, while it is highly desirable to maintain a balance between the two.

Quantum sensing [2–6] and imaging [7–9] offer a solution to these limitations, with applications spanning from fundamental physics [10, 11] to biological measurements [12–14], target detection [15–18], optical memory

readout [19, 20], and pattern recognition [21].

In quantum imaging, single-photon emitters have enabled super-resolution fluorescence microscopy [22–24], while label-free resolution enhancement has been achieved using position-momentum correlated photon pairs [25–27] and coincidence measurements, leveraging multi-photon quantum coherence [28, 29], which underpins quantum lithography [30]. Due to the intrinsic spatial and temporal correlations of photon pairs, uncorrelated external background [16, 27, 31, 32] can also be rejected.

Quantum techniques also enable new phase imaging schemes: spatial and polarization entanglement have been used for quantum holography [33–35], imaging with undetected photons [36–38], and S(1,1) nonlinear interferometry [39], which enables separation between the probing and detection wavelengths. Alternatively, quantum methods such as Hong-Ou-Mandel interferometry allow depth profiling via photon indistinguishability [40, 41]. However, these approaches do not enhance sensitivity beyond the shot-noise limit of their classical counterparts.

Phase supersensitivity can be achieved by exploiting  $N$ -photon entangled NOON states, which exhibit a de Broglie wavelength of  $\lambda/N$  [42]. While proof-of-principle experiments have been conducted using 2-photon entanglement—initially with raster-scanning systems [43, 44] and more recently in wide-field modalities [45]—practical implementations remain challenging due to the difficul-

ties in generating NOON states with  $N > 2$  and their susceptibility to optical losses. In general, lateral spatial resolution remains constrained by the biphoton correlation width, which is tied to maximizing the joint two-photon detection probability.

A different approach, called sub-shot-noise quantum imaging (SSNQI) [46–49], surpasses the sensitivity limit in weak object transmission measurements, ideally by a factor  $\sqrt{1-\tau}$  [50–54], where  $0 \leq \tau \leq 1$  is the sample transmittance. SSNQI exploits non-classical intensity correlations between two spatially separated beams [55]: one interacts with the object forming a noisy classical image, while the other serves as a quantum noise reference, which is subtracted from the object image. Recent advances have extended SSNQI to non-interferometric quantum-enhanced phase imaging (NIQPI) [56], where quantitative phase information is retrieved from intensity patterns using the transport-of-intensity equation (TIE) [57–59]. A similar non-interferometric approach was recently employed for biphoton state reconstruction [60].

The strength of SSNQI and NIQPI lies in their favorable operating conditions: they do not require phase stability as in interferometric techniques, operate rapidly with quasi single-shot first-order intensity measurements, and are completely scanning-free.

However, earlier demonstrations were limited by a significant trade-off between noise reduction and spatial resolution. Specifically, strong shot-noise suppression was achieved by maximizing the collection of correlated photon pairs using detection areas larger than the photon-pair transverse spatial correlation area. While this optimization enhanced noise reduction, it inevitably compromised spatial resolution, effectively acting as a low-pass filter and blurring fine details.

Here, we show that, contrary to prior assumptions, NIQPI’s resolution is not fundamentally constrained by such averaging. This breakthrough arises from the specific and favorable interplay between the features of SSNQI and the TIE-based reconstruction algorithm, enabling excellent quantum noise reduction while preserving fine details, with resolution virtually limited only by the numerical aperture of the imaging system.

Importantly, we demonstrate this quantum advantage in samples containing both phase and amplitude structures, achieving noise reduction exceeding 30%.

Finally, we report wide-field quantum-enhanced quantitative phase imaging of thin biological samples, achieving cellular and sub-cellular resolution. This opens a concrete perspective for immediate application and the potential development of commercial quantum imaging prototypes.

## NIQPI

The SSNQI and NIQPI protocols exploit the scheme depicted in Fig. 1a [56]. In a type-II nonlinear crystal pumped by a Gaussian coherent laser beam, spontaneous parametric down-conversion (SPDC) generates signal ( $s$ ) and idler ( $i$ ) beams, which become spatially separated at the crystal’s far-field (CFF), obtained at the focus of a lens in an  $f$ - $f$  configuration. Signal and idler photons are always generated in pairs along correlated and symmetric directions with respect to the pump propagation axis. This angular correlation translates into a transverse spatial correlation in the CFF, characterized by a correlation length  $l_{\text{CFF}}$  ( $l_{\text{CFF}} \approx 5 \mu\text{m}$  in our setup, approximately symmetric along both transverse directions). The corresponding correlation area,  $l_{\text{CFF}}^2$  in the other beam, is approximately four orders of magnitude smaller than the overall spot size of each beam. In the low-gain regime of SPDC, the intensity patterns of the  $s$ - and  $i$ -beams are each characterized by shot-noise spatial fluctuations with a white spatial spectrum, i.e., the shot-noise is equally present at all spatial frequencies. Furthermore, the shot-noise fluctuations of the two beams are almost identically correlated (at spatial frequencies larger than  $l_{\text{CFF}}$ ) across the entire spot size, a feature impossible to reproduce with classical light sources.

The signal beam probes the object placed near the CFF plane. An imaging system projects the CFF onto a low-noise, high quantum-efficiency charge-coupled device (CCD) camera with magnification  $M$ , yielding photon counts  $N_s(\mathbf{x}, dz)$  in the pixel with transverse coordinate  $\mathbf{x}$ , where  $dz$  denotes the distance of the object from the CFF along the propagation axis. Hereinafter, we will indicate by  $N'_s$ , with  $(')$ , the intensity measured with the object and  $N_s$  the one without the object. Simultaneously, the idler beam is directed onto a separate region of the detector, producing a photon-count distribution  $N_i(\mathbf{x})$ , which is used to subtract the quantum-correlated shot-noise from the measured intensity in the signal arm. These intensity correlations can be directly applied in the SSNQI protocol. In particular, the transmission of an object placed in the CFF plane,  $\tau(\mathbf{x})$ , is estimated as [49, 61]:

$$\hat{\tau}_Q(\mathbf{x}) = \frac{N'_s(\mathbf{x}, 0) - k_{\text{opt}}^{(\tau)} \delta N_i(\mathbf{x})}{\langle N_s(\mathbf{x}, 0) \rangle}. \quad (1)$$

The quantity  $\delta N_i(\mathbf{x}) = N_i(\mathbf{x}) - \langle N_i(\mathbf{x}) \rangle$  represents the fluctuation of photon counts in the correlated pixel of the  $i$ -arm and compensates for the fluctuation in the corresponding  $s$ -arm pixel. The factor  $k_{\text{opt}}^{(\tau)}$  is chosen to minimize the variance  $\langle \delta^2 \hat{\tau}_Q \rangle$ , taking into account imperfect correlations, and will be discussed later. It is straightforward to show that this estimator is unbiased, with  $\langle \hat{\tau}_Q(\mathbf{x}) \rangle = \tau(\mathbf{x})$ .

NIQPI, presented in [56], successfully applied SSNQI



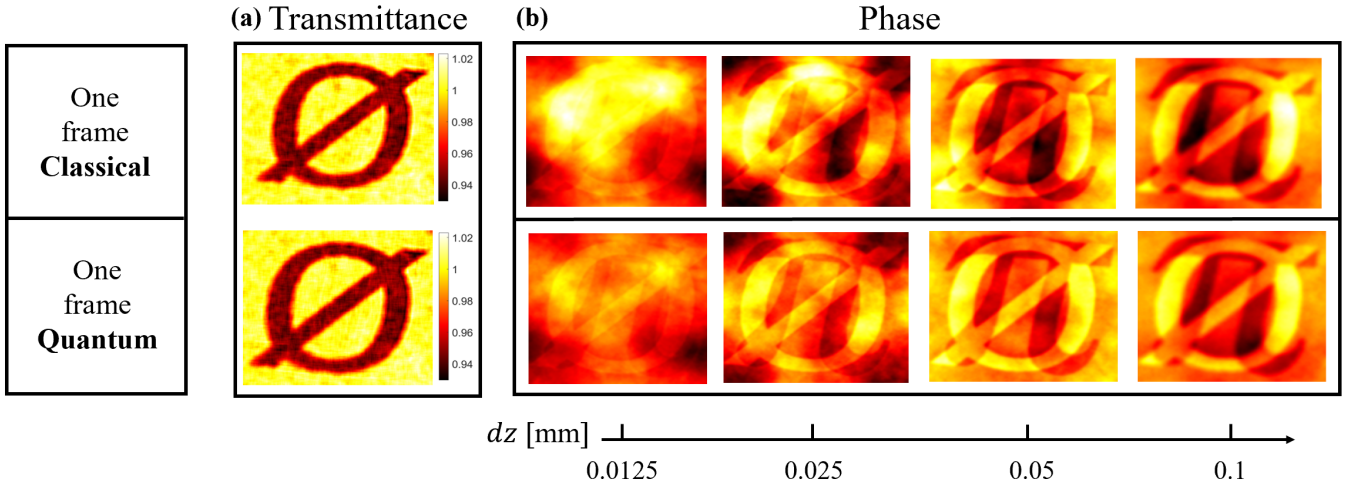


FIG. 2: *Experimental reconstruction of transmittance and phase object* (a) Transmittance estimations for classical and quantum single-frame images, processed with a factor  $\mathcal{D} = 3.8$ . The object's area occupies  $220 \times 220 \text{ pix}^2$  with a mean number of photon per pixel of 600. (b) Phase reconstruction at various defocus distances,  $dz$ , comparing classical and quantum single-frame approaches. The phase estimations at the smallest  $dz$  are: classical  $\pi = (-0.260 \pm 0.030)$  rad, quantum  $\pi = (-0.259 \pm 0.022)$  rad (theoretical  $\pi = (-0.226 \pm 0.006)$  rad); classical  $\varnothing = (0.365 \pm 0.020)$  rad, quantum  $\varnothing = (0.364 \pm 0.015)$  rad (theoretical  $\varnothing = (0.345 \pm 0.014)$  rad). Experimental uncertainties are obtained as mean errors calculated over  $10^3$  frames.

[56]:

$$I(\mathbf{x}, z) \mapsto N'_s(\mathbf{x}, z) - k_{\text{opt}}^{(\text{TIE})} \delta N_i(\mathbf{x}, 0), \quad (4)$$

where the number of photon counts,  $N$ , is considered in place of the intensities  $I$  since the two quantities are proportional, given a fixed detection time and area.

While previous experiments focused exclusively on pure-phase samples, extending the approach to realistic biological applications introduces additional complexities. Biological specimens typically feature regions dominated by phase variations with negligible absorption, alongside areas where phase and absorption effects co-exist. Accurately retrieving and distinguishing these two types of information is essential for a comprehensive characterization of both the structural and functional features of biological samples.

To address this general scenario, we employed an engineered test object composed of distinct phase and transmittance masks (Fig. 1b). The phase mask consists of the superposition of a pure phase structure featuring a  $\pi$ -shaped symbol and a  $\varnothing$ -shaped symbol (more information is provided in the Supplementary Document). The respective phase shifts are ( $\pi = -0.226 \pm 0.006$ ) rad and ( $\varnothing = 0.345 \pm 0.014$ ) rad relative to the background @810 nm, the degenerate wavelength of the SPDC process. Additionally, the  $\varnothing$ -shaped symbol exhibits a transmittance of approximately 0.94 relative to the flat of the Silica.

The TIE method inherently addresses these challenges by decoupling phase-induced intensity variations from those arising due to the non-uniform transmittance [59], thanks to the use of the intensity measurements acquired

at symmetrically defocused planes,  $I(\mathbf{x}, \pm dz)$ , as further described in the M&M section.

#### Quantum Advantage vs Spatial Resolution

The noise reduction factor (NRF), defined as  $\text{NRF} = \frac{\langle \delta^2(N_s - N_i) \rangle}{\langle N_s + N_i \rangle}$ , is a well-established quantifier of non-classical correlations and shot-noise suppression, comparing the residual fluctuations in the difference of photon counts (numerator) to the shot-noise level expected for classical states (denominator) [62–66]. For classical light, the NRF satisfies  $\text{NRF} \geq 1$ , while quantum-correlated states can reach values in the sub-shot-noise regime,  $0 \leq \text{NRF} < 1$ .

In the case of two correlated regions of a detector collecting SPDC photons, the NRF can be expressed as  $\text{NRF} = 1 - \eta_0 \eta_c(\mathcal{D})$ , where  $\eta_0$  is the single-channel detection efficiency, with the assumption of a balanced setup,  $\eta_s = \eta_i = \eta_0$ , and  $\eta_c(\mathcal{D})$  represents the collection efficiency of correlated photon pairs [47, 49]. The quantity  $\eta_c(\mathcal{D})$  is an increasing function of the ratio  $\mathcal{D} = \frac{L_{\text{det}}}{M \cdot l_{\text{CFF}}}$ , with  $L_{\text{det}}$  the linear size of the detector's integration area,  $M$  the system magnification, and  $l_{\text{CFF}}$  the correlation length in the crystal far-field. Further details about the estimation of  $\eta_0$  and  $\eta_c(\mathcal{D})$  are provided in the M&M section. When  $\mathcal{D} \gg 1$ , most of the correlated photon pairs are collected by two symmetric detection areas in the signal and idler beams, maximizing  $\eta_c(\mathcal{D}) \approx 1$ ; conversely, for  $\mathcal{D} \lesssim 1$ , only a fraction of the pairs are detected.

It is important to note that, while the spatial resolution  $r_{\text{CFF}}$  of the signal beam alone is inherently lim-

ited by the numerical aperture of the imaging system to  $r_{\text{CFF}} \approx 1.5 \mu\text{m}$  in our setup, noise subtraction in the intensity image is effective only on spatial scales larger than  $l_{\text{CFF}}$ , that is for  $\mathcal{D} \gtrsim 1$ . This introduces a fundamental trade-off between spatial resolution and quantum advantage in SSNQi for amplitude objects, based on the estimator in Eq. (1). This dependency has been extensively characterized in previous works [47, 49, 67]. Under the assumptions of quasi-Poissonian photon number statistics in each arm and high object transmittance  $\tau \approx 1$ , the optimization factor  $k_{\text{opt}}^{(\tau)}$  can be approximated as  $k_{\text{opt}}^{(\tau)}(\mathcal{D}) \approx 1 - \text{NRF} = \eta_0 \eta_c(\mathcal{D})$ , indicating the dependence on the resolution parameter  $\mathcal{D}$ . In practice,  $k_{\text{opt}}^{(\tau)}$  is calibrated through a preliminary characterization of the experimental NRF as a function of  $\mathcal{D}$  (see M&M).

At first glance, one might expect that the same resolution-related limitation would also affect the task of phase imaging via Eq. (2), since the noise reduction in intensity measurements follows the same principle outlined in Eq. (4). However, the main goal of this work is to demonstrate that this is not the case: the quantum advantage in phase retrieval is largely independent of the spatial resolution of the reconstructed images.

To understand why this is the case, it is essential to consider how intensity noise propagates into the retrieved phase profile. By examining Eq. (2), under the assumption that the finite-difference term  $I(\mathbf{x}, dz) - I(\mathbf{x}, -dz)$  is dominated by noise fluctuations  $\sigma(\mathbf{x})$ , and considering a nearly uniform illumination intensity  $I(\mathbf{x}, 0) \approx I_0$ , the equation simplifies to [68]:

$$-k \frac{\sigma(\mathbf{x})}{\sqrt{2} I_0 dz} = \nabla^2 \phi_{\text{noise}}(\mathbf{x}). \quad (5)$$

Considering the Fourier transform of both  $\sigma(\mathbf{x})$  and  $\phi_{\text{noise}}(\mathbf{x})$  yields:

$$\frac{k \tilde{\sigma}(\mathbf{q})}{4\pi^2 \sqrt{2} I_0 dz |\mathbf{q}|^2} = \tilde{\phi}_{\text{noise}}(\mathbf{q}), \quad (6)$$

where  $\tilde{\sigma}(\mathbf{q})$  and  $\tilde{\phi}_{\text{noise}}(\mathbf{q})$  denote the Fourier transforms of the intensity noise and the resulting phase noise, respectively, and  $\mathbf{q}$  represents the spatial frequency vector. In the case of shot-noise we can assume a flat spectrum,  $\tilde{\sigma}(\mathbf{q}) = \tilde{\sigma}$ , for  $\mathbf{q} \neq 0$ . The presence of the  $|\mathbf{q}|^2$  term in the denominator highlights that the phase noise in the TIE reconstruction is dominated by low spatial frequencies, i.e. by the slowly varying shot-noise fluctuations across the image. In contrast, high-frequency noise components, such as pixel-to-pixel shot-noise, are strongly suppressed by the intrinsic low-pass filtering nature of the TIE, and therefore have minimal impact on the retrieved phase. Incidentally, the remaining low-frequency components of the shot-noise are precisely those efficiently removed through quantum correlations, by the substitution in Eq. (4).

Since low spatial frequencies dominate the overall noise contribution in the retrieved phase, the optimal correction factor in Eq. (4) for phase estimation can be evaluated analogously to the amplitude case, but in the limit of a large integration area. In this regime,  $k_{\text{opt}}^{(\text{TIE})} = k_{\text{opt}}^{(\tau)}(\mathcal{D} \gg 1) \approx \eta_0$ , thus losing its strong dependence on the resolution of the acquired intensity images. Further details, particularly regarding the validity conditions of this approximation, are provided in the M&M section.

It is noteworthy to mention that the intrinsic suppression of high-frequency noise does not prevent the retrieval of high-resolution phase images. In fact, as it is clear from Eq. (2), in the direct-propagation problem, higher-frequency components of the phase object produce a stronger effect on the intensity. Thus, regions with rapid phase variations, i.e. high-frequency features, are usually reconstructed accurately despite the suppression introduced by solving the TIE [68].

These results are shown in Fig. 1c. The quantum advantage is quantified as the ratio between two Pearson correlation coefficients: one calculated using quantum-corrected phase images and the other using classical (shot-noise limited) phase images, each compared with a reference obtained by averaging  $10^3$  frames to eliminate residual shot-noise. The Pearson correlation coefficient  $\mathcal{C}$ , a widely used metric to evaluate the similarity between two images, is defined as:

$$\mathcal{C} = \frac{\sum_x (\phi_r(x) - \bar{\phi}_r) (\phi(x) - \bar{\phi})}{\sqrt{\text{Var}[\phi_r] \text{Var}[\phi]}}, \quad (7)$$

where  $\bar{\phi}$  and  $\text{Var}[\phi]$  denote the spatial mean and variance of the phase image  $\phi$ , respectively.

In the figure, the blue data points represent the experimental quantum advantage obtained using the optimization factor  $k_{\text{opt}}^{(\text{TIE})} = \eta_0$  in Eq. (4), with a single-channel overall detection efficiency estimated as  $\eta_0 \approx 0.7$ , while the red points indicate results obtained with  $k_{\text{opt}}^{(\tau)} = \eta_0 \eta_c(\mathcal{D})$ , used for transmittance measurements and previously employed for phase imaging in Ref. [56]. The shaded red and blue areas represent results from Fourier-optics simulations [69], showing good agreement with the experimental data, whereas the green area indicates the gain in the quantum advantage achievable with the new reconstruction strategy.

The data are displayed as a function of the defocusing distance  $dz$  and the resolution factor  $\mathcal{D}$ . We observe that using  $k_{\text{opt}}^{(\tau)}(\mathcal{D})$ , originally defined for amplitude imaging, in the context of phase estimation is counterproductive, leading to a reduced quantum advantage at small values of  $\mathcal{D}$ . In fact, at small  $\mathcal{D}$  the collection efficiency becomes  $\eta_c(\mathcal{D}) \ll 1$ , and  $k_{\text{opt}}^{(\tau)}(\mathcal{D}) \ll 1$ , resulting in quantum performance comparable to classical measurements. However, in amplitude SSNQi this choice still provides the optimal noise reduction, although modest, at small spatial scale [49, 56].

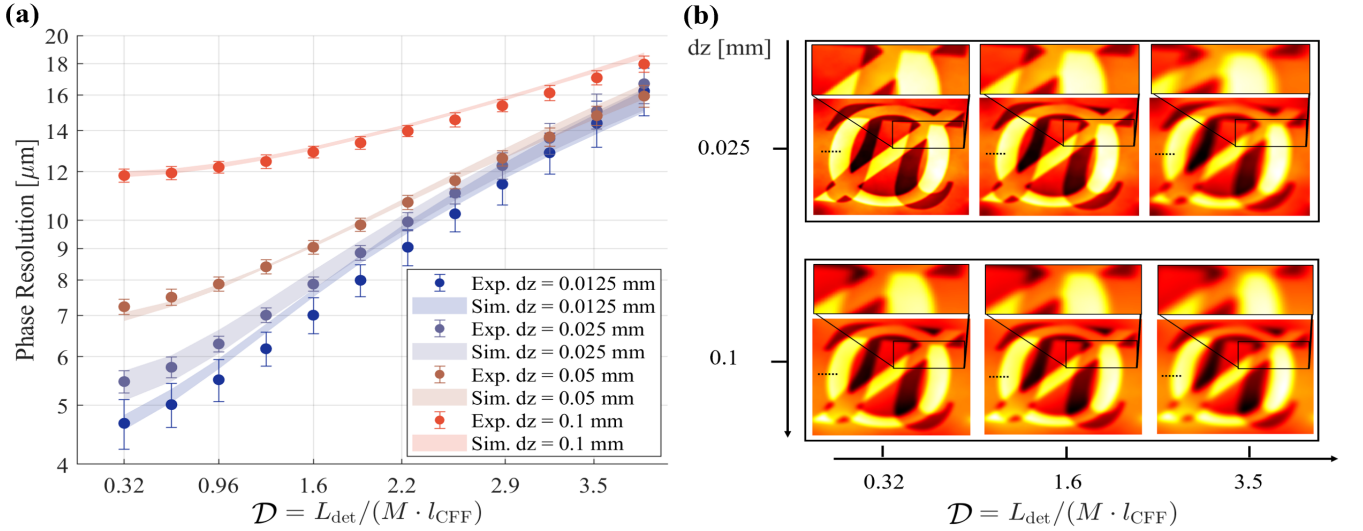


FIG. 3: *Phase resolution evaluation with the optimized correction factor  $k_{\text{TIE}}$*  (a) Experimental and simulated phase resolution as a function of the resolution factor  $\mathcal{D}$  for different defocus distances  $dz$ . The points correspond to experimental data for various  $dz$  values, while shaded areas represent theoretical predictions. As  $\mathcal{D}$  increases, the resolution worsens due to the larger effective pixel size, while smaller  $dz$  values allow better resolution. (b) Representative phase reconstructions for two different defocus distances ( $dz = 0.025$  mm and  $dz = 0.1$  mm) and three different  $\mathcal{D}$  values. Insets show magnified regions of the sample for a better qualitative evaluation of the phase resolution changes.

In contrast, since high-frequency fluctuations are inherently suppressed in NIQPI through the solution of the TIE, it is more convenient to apply the factor  $k_{\text{opt}}^{(\text{TIE})} \approx \eta_0$ , which more effectively optimizes noise suppression at low spatial frequencies, even to high-resolution intensity images.

The quantum advantage is most pronounced at small defocus distances  $dz$ , where the intensity variations induced by phase propagation are weaker. In this regime, quantum noise suppression becomes particularly impactful, achieving an advantage close to 30%. We recall that, in the opposite regime of large refocusing distance, the finite-difference approximation is poor, thereby reducing both the resolution and the quantitative accuracy of phase estimation [56].

In Fig. 2, we present the classical and quantum reconstructions of both the phase and transmittance profiles. The reconstructions clearly demonstrate the effectiveness of the method in separating transmittance and phase information, as well as highlighting the quantum advantage. For the transmittance reconstruction a resolution parameter  $\mathcal{D} = 3.8$ , corresponding to a spatial resolution of  $18 \mu\text{m}$ , was used to maximize the collection efficiency  $\eta_c(\mathcal{D})$ . This choice enabled the achievement of an NRF of 0.45 and a quantum advantage of 25% in the standard deviation of the reconstructed amplitude. Note that, given the transmittance level of the mask,  $\tau = 0.94$ , and the large photon counts, the classical image already provides good retrieval, which limits the visual perception of the quantum advantage in the reconstructed image. How-

ever, this does not diminish the significant quantum advantage observed in the measured uncertainty over the transmittance.

Conversely, the phase reconstruction reveals a visual quantum advantage. The phase's values estimated for the smallest defocus distance  $dz$ , where the approximation in Eq. (3) is most accurate, are listed in the caption. They show a good agreement with theoretical predictions and a reduced uncertainty for the quantum case.

Fig. 3 presents a quantitative evaluation of the spatial phase resolution achieved with the new  $k_{\text{opt}}^{(\text{TIE})}$ -based phase retrieval strategy, as a function of the effective resolution of the intensity images,  $\mathcal{D}$ . The results, shown in Fig. 3a, are reported for different defocus distances  $dz$ . Each data point represents the experimental resolution extracted from phase images averaged over  $10^3$  frames to eliminate residual shot-noise. The shaded area indicates the theoretical resolution limit achievable with the current optical system. Fig. 3b displays representative phase reconstructions, also averaged over  $10^3$  frames, for two defocus distances,  $dz = 0.025$  mm and  $dz = 0.1$  mm, at three different values of  $\mathcal{D}$ . Rectangular regions within each phase image are magnified to illustrate resolution variations more clearly.

To quantify the spatial resolution, horizontal phase profiles were extracted along the dashed lines indicated in Fig. 3b. These profiles were then fitted using an error function (Edge Spread Function, ESF), allowing the spatial resolution to be defined as  $r_{\text{phase}} = 2\sqrt{2\ln(2)}w$ , where  $w$  denotes the characteristic width parameter ob-

tained from the ESF fit (see M&M for further details). The uncertainty associated with the resolution measurements was estimated from the 95% confidence interval of the parameter  $w$ . As clearly shown by the curves in Fig. 3a, decreasing the defocus distance  $dz$  improves the resolution by enabling a more accurate approximation of the derivative term in Eq. (2), ultimately achieving a phase spatial resolution of approximately  $4\mu\text{m}$  for  $dz = 0.0125\text{ mm}$  and for the minimal integration length  $L_{\text{det}}$  of the physical pixel, that correspond to  $\mathcal{D} = 0.32$ . Conversely, increasing the integration area leads to a loss of resolution, where all the curves approach the same asymptotic behavior, with a spatial resolution of the phase images around  $18\mu\text{m}$ , as achieved in our previous work [56]. As mentioned this strongly limited practical applications of this technique. In the present work, this limitation was overcome by fully exploiting the unique properties of TIE noise propagation at high spatial frequencies.

The overall spatial resolution at the micrometer scale and the ability of the method to operate effectively in the presence of both phase and absorption contrast demonstrate the readiness of this method for practical application, in particular in biological microscopy. In the following we proceed to apply the technique to biological samples to practically demonstrate this use.

### Biological Sample

We investigated unstained sea urchin ova, chosen for their natural transparency and intrinsic phase contrast. The samples were obtained from an industrial preparation with minimal staining, preserving the native optical properties of the cells.

Fig. 4 presents wide-field phase reconstructions of ova at different developmental stages: from unfertilized eggs (top row), to fertilized eggs in early cleavage stages (middle row), to advanced embryonic forms (bottom row). These three biological conditions were imaged under different experimental settings. The defocus distances used in the TIE reconstruction were  $dz = 10\mu\text{m}$ ,  $5\mu\text{m}$ , and  $5\mu\text{m}$ , respectively, and the average number of detected photons per pixel was approximately 1000, 300, and 600 for the three samples.

The first column displays the reference phase image obtained by averaging 100 independent frames in order to eliminate any shot-noise. The second column shows the phase reconstruction from a single frame without any quantum correction. The third column presents the quantum-enhanced phase image obtained by the substitution in Eq. (4) using the optimized correction factor  $k_{\text{opt}}^{(\text{TIE})} = \eta_0$ .

The quantum-corrected images demonstrate a visible improvement in contrast and noise suppression compared to the classical single-shot reconstructions, approaching

100 frames average    Classical frame    Quantum frame

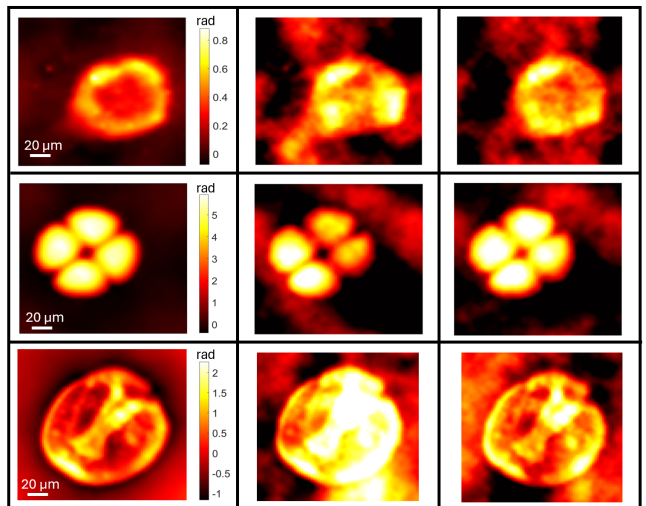


FIG. 4: *Biological quantum phase imaging with high resolution.* (Left column) Phase images obtained by averaging 100 frames, serving as a shot-noise-free reference. (Middle column) Classical single-shot phase images, affected by shot-noise. (Right column) Quantum-corrected single-shot phase images, showing visibly improved quality and enhanced contrast compared to the classical case. Each row corresponds to a different biological sample, and the same color scale is used within each row. The scale bar corresponds to  $20\mu\text{m}$ .

the quality of the 100-frame averaged images. In particular, a quantum advantage between 5% and 20% was measured across different biological samples. These results highlight both the robustness of the method in the presence of low signal levels and its capacity to provide high-fidelity phase reconstructions in biologically relevant conditions.

### CONCLUSION

We have demonstrated a powerful sub-shot-noise technique in the domain of phase imaging, which does not suffer from any trade-off between spatial resolution and quantum gain in sensitivity. This enables the development of a microscope with diffraction-limited resolution and sub-shot-noise enhancement. In the microscopic system presented here, although we reach micrometer-scale resolution, the minimal achievable resolution does not yet match the diffraction limit of the imaging system. This discrepancy is due to technical limitations, the most relevant being the imperfect approximation of the derivative in Eq. (3) for the chosen value of  $dz$ . Further improvements could be obtained by multi-distance approaches to TIE, which combine intensity measurements at both small and large defocus distances [70], by employing structured illumination techniques [71] or simply by considering a smaller defocusing distance. This last

approach would be possible just by a finer control of the translator stages. Additionally, in our setup, the diffraction limit is close to the physical pixel size of the detector, making it challenging to precisely evaluate the resolution near the theoretical limit.

To demonstrate the applicability of our quantum-enhanced phase imaging method to real-world biological systems, we performed phase imaging of cells with details of a few micrometers, clearly showing less noise artifacts with respect to the classical measurement. Finally, our method is scanning free, requires only two shots for complete phase retrieval and do not need complicated interferometric setups. Filling the gap between proof-of-concept and real word applicability, this work represents an important step for the quantum sensing technology, where only a very limited number of protocols have reached an application level like ours. Several applications can already be envisaged whenever high illumination level can damage the sample or in fast imaging where the illumination level for the single frame should remain limited.

## MATERIALS AND METHODS

### Experimental layouts

The experimental setup is based on a continuous-wave (CW) laser source (OBIS405 Coherent) operating at a wavelength  $\lambda_p = 405$  nm with a beam width of  $w = 0.5$  mm. Although the source is CW, it is triggered in a pulsed mode synchronized with the camera's acquisition, with a maximum output power of 100 mW. The pump beam generates photon pairs via spontaneous parametric down-conversion (SPDC) in a 1.5 cm-long, type-II beta-barium borate (BBO) nonlinear crystal with transverse dimensions of  $0.8 \times 0.8$  cm<sup>2</sup>. The down-converted photons are filtered by an interferential filter centered at  $800 \pm 20$  nm, selecting only photons near the degenerate wavelength  $\lambda_d = 810$  nm.

Spatial correlations are established at the crystal far-field (CFF) plane, formed by a lens with focal length  $f = 1$  cm. A second imaging lens with focal length  $f = 1.6$  cm projects the far-field onto the CCD detection plane with a magnification factor of  $M = 8$ . The detector is a Pixis 400BR Excelon CCD camera (Princeton Instruments) with a  $1024 \times 1024$  pixel array and  $13 \mu\text{m}$  pixel pitch. The pixel size on the object plane is approximately  $1.5 \mu\text{m}$ . The camera operates in linear mode with high quantum efficiency ( $> 95\%$ ), low electronic noise, and full fill factor.

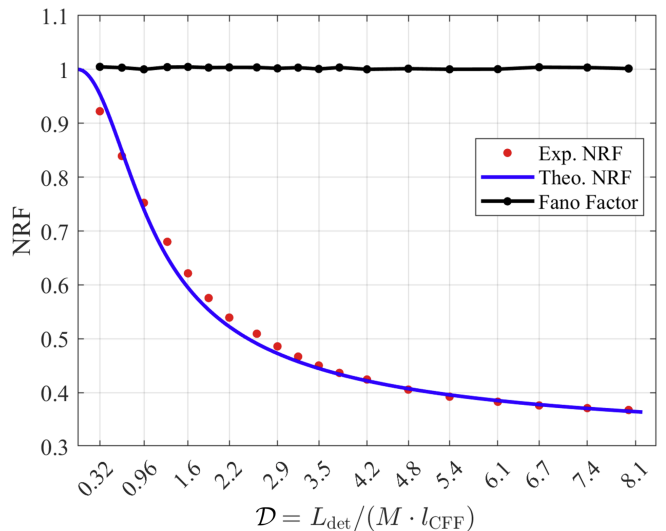


FIG. 5: *Experimental and theoretical behavior of NRF as a function of the parameter  $\mathcal{D}$ . Red points represent measured NRF values, the blue curve corresponds to theoretical predictions based on Eq. (9), and black points indicate the Fano factor, confirming Poissonian photon statistics.*

### Characterization of Twin-Beams by NRF

We assume, as a good approximation, a Gaussian spatial transverse correlation in the CFF,  $\propto (2\pi\sigma^2)^{-1/2} e^{-(\mathbf{x}_i + \mathbf{x}_s)^2 / 2\sigma^2}$ : if a signal photon is detected in the position  $\mathbf{x}_s$  the twin idler photon will be detected according to that Gaussian probability around  $\mathbf{x}_i = -\mathbf{x}_s$ . The conditional detection efficiency  $\eta_c$  depends on the pixel size (or the effective integration area) projected at the CFF,  $L_{\text{det}}/M$ , where  $L_{\text{det}}$  is the linear size of the integration area and  $M$  is the magnification of the imaging system. It also depends on any misalignment,  $\Delta$ , between the two pixels relative to their optimal positions. Specifically,  $\eta_c$  can be modeled as

$$\eta_c = \left( \frac{L_{\text{det}}}{M} \right)^{-2} \int_{\mathcal{A}} d\mathbf{x}_s \int_{\mathcal{A}} d\mathbf{x}_i \frac{1}{\sqrt{2\pi}\sigma} e^{-\frac{(\mathbf{x}_i + \mathbf{x}_s + \Delta)^2}{2\sigma^2}} \quad (8)$$

where the integration area is  $\mathcal{A} = L_{\text{det}}/M \times L_{\text{det}}/M$ . The full width at half maximum (FWHM) of the correlation function is given by  $l_{\text{CFF}} = 2\sqrt{2 \ln(2)} \sigma$ .

By changing variables in Eq. (8), one finds that  $\eta_c$  depends only on two dimensionless parameters: the normalized detector linear size and the misalignment, both expressed in units of the correlation length. That is,  $\eta_c(\mathcal{D}, \epsilon)$ , where  $\mathcal{D} = L_{\text{det}}/(M \cdot l_{\text{CFF}})$  and  $\epsilon = \Delta/l_{\text{CFF}}$ . For simplicity, we assume equal misalignment in both spatial directions, so that  $\Delta$  is treated as a scalar. The conditional efficiency  $\eta_c(\mathcal{D}, \epsilon)$  and the detection efficiency  $\eta_0$  were estimated through measurements of the Noise Reduction Factor (NRF), defined as  $\text{NRF} = \frac{\langle \delta^2(N_s - N_i) \rangle}{\langle N_s + N_i \rangle}$ .

For SPDC light, the NRF can be approximated by:

$$\text{NRF} \approx 1 - \eta_0 \eta_c(\mathcal{D}, \epsilon). \quad (9)$$

Fig. 5 shows the experimentally measured NRF values (red dots) alongside the theoretical prediction (blue curve). The NRF was measured as a function of  $\mathcal{D}$ , by varying  $L_{\text{det}}$ . A fit of the experimental data to Eq. (9) was performed using two free parameters: the misalignment  $\epsilon$  and the single-channel detection efficiency  $\eta_0$ . The fit yielded  $\epsilon = 0.2$  and  $\eta_0 = 0.7$ , in good agreement with the experimental data. These parameters were used for the results shown in the main text.

The black points in the figure represent the Fano factor,  $F = \frac{\langle \delta^2 N \rangle}{\langle N \rangle}$ , which remains close to one for all values of  $\mathcal{D}$ , confirming that the photon statistics is in the Poissonian regime.

### TIE with phase and amplitude

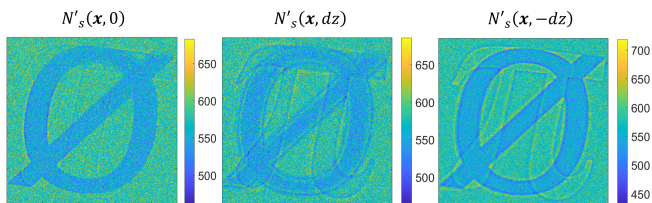


FIG. 6: *Photon counts with the object placed at three distances.* (Left panel) Photon counts recorded with the object positioned at the focal plane of the imaging system. In this case, only the transmittance mask ( $\emptyset$ ) is visible. When the object is moved to defocused planes at distances  $\pm dz$  (middle and right panel), phase variations induce additional intensity modulations, resulting in an overlap of phase and amplitude effects. Nevertheless, the TIE allows decoupling of these contributions, enabling the quantitative and unique retrieval of the sample's phase profile.

In Fig. 6, the single-frame photon count images  $N'_s(\mathbf{x}, z)$  are shown for three different axial positions of the object relative to the CFF plane:  $z = 0$  (left),  $z = +dz$  (center), and  $z = -dz$  (right) (with  $dz = 0.05$  mm). When the object is located at the nominal focus ( $z = 0$ ), only the amplitude (non-uniform transmittance) features are visible in the intensity distribution. In contrast, at defocused positions ( $\pm dz$ ), phase-induced propagation effects become evident, revealing the  $\pi$ -shaped phase structure superimposed on the amplitude modulation of the  $\emptyset$ -sign and its phase. Notably, the out-of-focus images exhibit overlapping features from both the amplitude and phase masks, underscoring the need for proper decoupling via the TIE to retrieve the pure phase profile.

A way to solve the TIE in Eq. (2) with the measured photon counts is to adopt the so-called Teague's assump-

tion [57], introducing an auxiliary function  $\psi(\mathbf{x})$  so that

$$I(\mathbf{x}, 0) \nabla \phi(\mathbf{x}, 0) = \nabla \psi(\mathbf{x}). \quad (10)$$

According to Helmholtz's theorem, the vector field  $I(\mathbf{x}, 0) \nabla \phi(\mathbf{x}, 0)$  can be decomposed into an irrotational component and a solenoidal component:  $I(\mathbf{x}, 0) \nabla \phi(\mathbf{x}, 0) = \nabla \psi + \nabla \times \mathbf{A}$ , where  $\psi$  is a scalar potential and  $\mathbf{A}$  is a vector potential. It follows that Teague's assumption holds if the transverse flux  $I(\mathbf{x}, 0) \nabla \phi(\mathbf{x}, 0)$  is irrotational. It has been shown that the irrotational approximation is valid if the in-focus intensity distribution is nearly uniform [59]. In this case, the phase discrepancy resulting from Teague's auxiliary function is essentially negligible. However, when the measured sample exhibits low transmittance, the phase discrepancy may be relatively large and cannot be neglected. In our case, we consider a relatively high transmittance profile (see Fig. 1b), so we can safely use Teague's assumption. The validity of the approximation is confirmed *a posteriori* by the correct recovery of the phase values, as presented in Fig. 2.

Performing the substitution suggested in Eq. (10) into Eq. (2) results in the following Poisson differential equation:

$$-k \frac{\partial}{\partial z} I(\mathbf{x}, z) = \nabla_{\mathbf{x}}^2 \psi(\mathbf{x}). \quad (11)$$

The solution to this equation is known, allowing the auxiliary function  $\psi(\mathbf{x})$  introduced by Teague to be determined. Subsequently, a second Poisson equation, directly obtained from Eq. (10), namely

$$\nabla \cdot [I(\mathbf{x}, 0)^{-1} \nabla \psi(\mathbf{x})] = \nabla_{\mathbf{x}}^2 \phi(\mathbf{x}), \quad (12)$$

enables the reconstruction of a unique phase profile  $\phi(\mathbf{x})$ , even in the presence of a weakly absorbing mask. This is done under Dirichlet boundary conditions, where the phase is set to zero at the borders of the reconstructed image.

### Phase resolution

#### Phase resolution enhancement

A core aspect of this work is the demonstrated resolution enhancement, as shown in Fig. 3. This improvement stems from the suppression of high-frequency noise via the solution of the TIE, as described in Eq. (6). A visual explanation of this mechanism is provided in the inset images within the plot shown in Fig. 7.

The central inset illustrates a typical noise pattern  $\sigma(\mathbf{x})$  ( $220 \times 220$   $\text{pix}^2$ ), characterized by Poissonian shot-noise that affects the raw intensity measurements. The lower left panel shows the low-frequency component

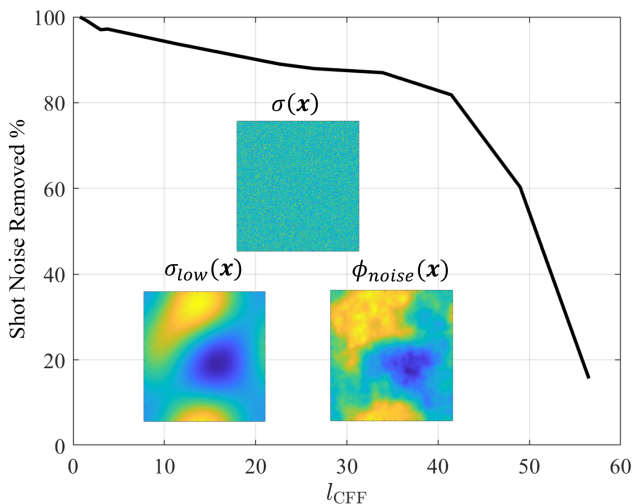


FIG. 7: *Visualization of noise suppression in phase retrieval with  $k_{TIE}$  estimator.* The plot shows the percentage of shot-noise removed as a function of correlation length  $l_{CFF}$ . Insets show: (top) experimental Poissonian noise pattern  $\sigma(\mathbf{x})$ , (bottom left) its low-frequency component  $\sigma_{low}(\mathbf{x})$ , and (bottom right) the resulting phase noise  $\phi_{noise}(\mathbf{x})$  after TIE processing.

$\sigma_{low}(\mathbf{x})$ , obtained by spatial filtering to remove high-frequency content and reveal only slowly varying fluctuations. The right panel displays the corresponding phase noise  $\phi_{noise}(\mathbf{x})$ , clearly showing that the dominant contribution to phase noise arises from low spatial frequencies. These components mainly affect broad regions of the retrieved phase image, approximately  $100 \times 100$  pixels in size.

The main plot in Fig. 7 reports simulation results evaluating the effectiveness of the TIE-based quantum method in suppressing phase noise as a function of the correlation length  $l_{CFF}$ . For simplicity a uniform detection efficiency  $\eta_0 = 1$  is considered. In the simulation, starting from a noise distribution  $\sigma(\mathbf{x})$ , a modified distribution  $\sigma'(\mathbf{x})$  is generated by redistributing photon counts across neighboring pixels using a 2D Gaussian kernel with a FWHM of  $l_{CFF}$ , modeling the spatial spread of the correlations. From the corrected intensity  $\sigma(\mathbf{x}) - k_{opt}^{(TIE)} \sigma'(\mathbf{x})$  the phase noise is retrieved solving the TIE and the resulting noise  $\phi_{noise}(\mathbf{x})$  is analyzed.

The curve shows the percentage of shot-noise removed as a function of  $l_{CFF}$ . When the correlation length is small,  $l_{CFF} < 30 \mu\text{m}$ , the TIE efficiently suppresses almost all of the noise. In particular, the experimentally estimated value  $l_{CFF} \approx 5 \mu\text{m}$  lies within this highly effective regime. However, as  $l_{CFF}$  increases beyond  $40 \mu\text{m}$ , the correlated noise begins to affect lower spatial frequencies, which are not suppressed by the TIE, and the quantum correction becomes less effective, leaving a substantial residual noise in the phase image.

### Phase resolution evaluation

To evaluate the spatial resolution of our imaging system, we analyze intensity profiles extracted along a line perpendicular to the edge of the phase samples averaged over  $10^3$  frames, in order to eliminate any shot-noise. These intensity profiles are fitted using an error function (Edge Spread Function, ESF) centered at position  $x_0$ :

$$\text{ESF}(x) = \frac{a}{2} \text{erf} \left( \frac{x - x_0}{\sqrt{2} w} \right) + b \quad (13)$$

where  $a$  and  $b$  are fitting coefficients, and  $w$  represents the characteristic width parameter of the transition region. Differentiating the ESF provides the Gaussian Line Spread Function (LSF):

$$\text{LSF}(x) = \frac{d\text{ESF}(x)}{dx} = \frac{a}{w\sqrt{2\pi}} \exp \left[ -\frac{(x - x_0)^2}{2w^2} \right] \quad (14)$$

The spatial resolution of the system is defined by the FWHM of the LSF, given by:

$$r_{\text{phase}} = 2\sqrt{2 \ln(2)} w \quad (15)$$

To quantify the uncertainty, we first determine the 95% confidence interval for the fitted parameter  $w$ , indicated as  $[w_{\text{sub}}, w_{\text{sup}}]$ . The standard error for  $w$  is then approximated as  $se_w = (w_{\text{sup}} - w_{\text{sub}})/3.92$  according to the  $z$ -test. Consequently, the standard error of the resolution  $R$  is calculated as:

$$se_r = \sqrt{2 \ln(2)} \frac{(w_{\text{sup}} - w_{\text{sub}})}{1.96} \quad (16)$$

### ACKNOWLEDGMENTS

The authors are particularly grateful to Silvania F. Pereira for her helpful discussions and valuable suggestions for improving the paper. This work has received funding from the European Union's through the following Projects: Horizon 2020 Research and Innovation Action under Grant Agreement Qu-Test (HORIZON-CL4-2022-QUANTUM-05-SGA); Next Generation EU, Missione 4 Componente 1 CUP C63C22000830006-Bando a Cascata Spoke Fondazione Bruno Kessler-M4C2I.1.3.-NQSTI, and from the European Defence Fund (EDF) under grant agreement 101103417 EDF-2021-DIS-RDIS-ADEQUADE (Funded by the European Union). Views and opinions expressed are however those of the author(s) only and do not necessarily reflect those of the European Union or the European Commission. Neither the European Union nor the granting authority can be held responsible for them.

## AUTHOR CONTRIBUTIONS

GO, IRB and AP devised the scheme of high resolution NIQPI. AP, GO and IRB developed the software for simulations and data analysis. The experiment and the data analysis have been carried out by AP with the help of IRB. IRB and AP wrote the paper with the contribution of all the Authors. The non-biological sample has been designed, fabricated and characterized by SS. IRB and MG are equally last co-Authors. IRB supervised the project together with MG who is the director of the Research Sector in which the work has been developed.

---

\* Electronic address: [i.ruoberchera@inrim.it](mailto:i.ruoberchera@inrim.it)

- [1] Y. Park, C. Depeursinge, and G. Popescu, *Nature Photonics* **12**, 578 (2018), <https://doi.org/10.1038/s41566-018-0253-x>, URL <https://doi.org/10.1038/s41566-018-0253-x>.
- [2] S. Pirandola, B. R. Bardhan, T. Gehring, C. Weedbrook, and S. Lloyd, *Nature Photonics* **12**, 724 (2018), ISSN 1749-4893, URL <https://doi.org/10.1038/s41566-018-0301-6>.
- [3] C. L. Degen, F. Reinhard, and P. Cappellaro, *Rev. Mod. Phys.* **89**, 035002 (2017), URL <https://link.aps.org/doi/10.1103/RevModPhys.89.035002>.
- [4] G. Petrini, E. Moreva, E. Bernardi, P. Traina, G. Tomagra, V. Carabelli, I. P. Degiovanni, and M. Genovese, *Advanced Quantum Technologies* **3**, 2000066 (2020), URL <https://onlinelibrary.wiley.com/doi/abs/10.1002/qute.202000066>.
- [5] C. Lee, B. Lawrie, R. Pooser, K.-G. Lee, C. Rockstuhl, and M. Tame, *Chemical Reviews* **121**, 4743 (2021), ISSN 0009-2665, URL <https://doi.org/10.1021/acs.chemrev.0c01028>.
- [6] E. Polino, M. Valeri, N. Spagnolo, and F. Sciarrino, *AVS Quantum Science* **2**, 024703 (2020), URL <https://doi.org/10.1116/5.0007577>.
- [7] H. Defienne, W. P. Bowen, M. Chekhova, G. B. Lemos, D. Oron, S. Ramelow, N. Treps, and D. Faccio, *Nature Photonics* **18**, 1024 (2024), URL <https://doi.org/10.1038/s41566-024-01516-w>.
- [8] I. R. Berchera and I. P. Degiovanni, *Metrologia* **56**, 024001 (2019), URL <https://doi.org/10.1088/2F1681-7575/2Faaf7b2>.
- [9] M. Genovese, *Journal of Optics* **18**, 073002 (2016), URL <https://doi.org/10.1088/2F2040-8978/2F18/2F7%2F073002>.
- [10] J. Aasi et al., *Nature Photonics* **7**, 613 EP (2013), URL <https://doi.org/10.1038/nphoton.2013.177>.
- [11] S. T. Pradyumna, E. Losero, I. Ruo-Berchera, P. Traina, M. Zucco, C. S. Jacobsen, U. L. Andersen, I. P. Degiovanni, M. Genovese, and T. Gehring, *Communications Physics* **3**, 104 (2020), ISSN 2399-3650, URL <https://doi.org/10.1038/s42005-020-0368-5>.
- [12] M. A. Taylor, J. Janousek, V. Daria, J. Knittel, B. Hage, H.-A. Bachor, and W. P. Bowen, *Phys. Rev. X* **4**, 011017 (2014), URL <https://link.aps.org/doi/10.1103/PhysRevX.4.011017>.
- [13] C. A. Casacio, L. S. Madsen, A. Terrasson, M. Waleed, K. Barnscheidt, B. Hage, M. A. Taylor, and W. P. Bowen, *Nature* **594**, 201 (2021).
- [14] G. Petrini, G. Tomagra, E. Bernardi, E. Moreva, P. Traina, A. Marcantoni, F. Picollo, K. Kvaková, P. Cígler, I. P. Degiovanni, et al., *Advanced Science* **9**, 2202014 (2022), URL <https://onlinelibrary.wiley.com/doi/abs/10.1002/adv.202202014>.
- [15] S.-H. Tan, B. I. Erkmen, V. Giovannetti, S. Guha, S. Lloyd, L. Maccone, S. Pirandola, and J. H. Shapiro, *Phys. Rev. Lett.* **101**, 253601 (2008), URL <https://link.aps.org/doi/10.1103/PhysRevLett.101.253601>.
- [16] E. D. Lopaeva, I. Ruo Berchera, I. P. Degiovanni, S. Olivares, G. Brida, and M. Genovese, *Phys. Rev. Lett.* **110**, 153603 (2013), URL <https://link.aps.org/doi/10.1103/PhysRevLett.110.153603>.
- [17] Z. Zhang, S. Mouradian, F. N. C. Wong, and J. H. Shapiro, *Phys. Rev. Lett.* **114**, 110506 (2015), URL <https://link.aps.org/doi/10.1103/PhysRevLett.114.110506>.
- [18] R. Gallego Torromé and S. Barzanjeh, *Progress in Quantum Electronics* **93**, 100497 (2024), ISSN 0079-6727, URL <https://www.sciencedirect.com/science/article/pii/S0079672723000460>.
- [19] G. Ortolano, E. Losero, S. Pirandola, M. Genovese, and I. Ruo-Berchera, *Science Advances* **7**, eabc7796 (2021), <https://www.science.org/doi/pdf/10.1126/sciadv.abc7796>, URL <https://www.science.org/doi/abs/10.1126/sciadv.abc7796>.
- [20] G. Ortolano, P. Boucher, I. P. Degiovanni, E. Losero, M. Genovese, and I. Ruo-Berchera, *Science Advances* **7**, eabm3093 (2021), <https://www.science.org/doi/pdf/10.1126/sciadv.abm3093>, URL <https://www.science.org/doi/abs/10.1126/sciadv.abm3093>.
- [21] G. Ortolano, C. Napoli, C. Harney, S. Pirandola, G. Leonetti, P. Boucher, E. Losero, M. Genovese, and I. Ruo-Berchera, *Phys. Rev. Appl.* **20**, 024072 (2023), URL <https://link.aps.org/doi/10.1103/PhysRevApplied.20.024072>.
- [22] D. Gatto Monticone, K. Katamadze, P. Traina, E. Moreva, J. Forneris, I. Ruo-Berchera, P. Olivero, I. P. Degiovanni, G. Brida, and M. Genovese, *Phys. Rev. Lett.* **113**, 143602 (2014), URL <https://link.aps.org/doi/10.1103/PhysRevLett.113.143602>.
- [23] O. Schwartz and D. Oron, *Phys. Rev. A* **85**, 033812 (2012), URL <https://link.aps.org/doi/10.1103/PhysRevA.85.033812>.
- [24] R. Tenne, U. Rossman, B. Rephael, Y. Israel, A. Krupinski-Ptaszek, R. Lapkiewicz, Y. Silberberg, and D. Oron, *Nature Photonics* **13**, 116 (2019), ISSN 1749-4893, URL <https://doi.org/10.1038/s41566-018-0324-z>.
- [25] E. Toninelli, P.-A. Moreau, T. Gregory, A. Mihalyi, M. Edgar, N. Radwell, and M. Padgett, *Optica* **6**, 347 (2019), URL <https://opg.optica.org/optica/abstract.cfm?URI=optica-6-3-347>.
- [26] H. Defienne, P. Cameron, B. Ndagano, A. Lyons, M. Reichert, J. Zhao, A. R. Harvey, E. Charbon, J. W. Fleischer, and D. Faccio, *Nature Communications* **13**, 3566 (2022).
- [27] Y. Zhang, Z. He, X. Tong, D. C. Garrett, R. Cao, and L. V. Wang, *Science Advances* **10**, eadk1495 (2024), <https://www.science.org/doi/pdf/10.1126/sciadv.adk1495>,

- URL <https://www.science.org/doi/abs/10.1126/sciadv.adk1495>.
- [28] M. D'Angelo, A. Mazzilli, F. V. Pepe, A. Garuccio, and V. Tamma, *Scientific Reports* **7**, 2247 (2017).
  - [29] M. Unternährer, B. Bessire, L. Gasparini, M. Perenzoni, and A. Stefanov, *Optica* **5**, 1150 (2018), URL <https://opg.optica.org/optica/abstract.cfm?URI=optica-5-9-1150>.
  - [30] M. D'Angelo, M. V. Chekhova, and Y. Shih, *Phys. Rev. Lett.* **87**, 013602 (2001), URL <https://link.aps.org/doi/10.1103/PhysRevLett.87.013602>.
  - [31] H. Defienne, M. Reichert, J. W. Fleischer, and D. Faccio, *Science Advances* **5**, eaax0307 (2019), <https://www.science.org/doi/pdf/10.1126/sciadv.aax0307>, URL <https://www.science.org/doi/abs/10.1126/sciadv.aax0307>.
  - [32] T. Gregory, P.-A. Moreau, E. Toninelli, and M. J. Padgett, *Science advances* **6**, eaay2652 (2020).
  - [33] S. Töpfer, M. G. Basset, J. Fuenzalida, F. Steinlechner, J. P. Torres, and M. Gräfe, *Science Advances* **8**, eabl4301 (2022), <https://www.science.org/doi/pdf/10.1126/sciadv.abl4301>, URL <https://www.science.org/doi/abs/10.1126/sciadv.abl4301>.
  - [34] A. N. Black, L. D. Nguyen, B. Braverman, K. T. Crampton, J. E. Evans, and R. W. Boyd, *Optica* **10**, 952 (2023), URL <https://opg.optica.org/optica/abstract.cfm?URI=optica-10-7-952>.
  - [35] H. Defienne, B. Ndagano, A. Lyons, and D. Faccio, *Nature Physics* **17**, 591 (2021), ISSN 1745-2481, URL <https://doi.org/10.1038/s41567-020-01156-1>.
  - [36] G. B. Lemos, V. Borish, G. D. Cole, S. Ramelow, R. Lapkiewicz, and A. Zeilinger, *Nature* **512**, 409 EP (2014), URL <https://doi.org/10.1038/nature13586>.
  - [37] I. Kviatkovsky, H. M. Chrzanowski, E. G. Avery, H. Bartolomaeus, and S. Ramelow, *Science Advances* **6**, eabd0264 (2020), <https://www.science.org/doi/pdf/10.1126/sciadv.abd0264>, URL <https://www.science.org/doi/abs/10.1126/sciadv.abd0264>.
  - [38] A. Vallés, G. Jiménez, L. J. Salazar-Serrano, and J. P. Torres, *Phys. Rev. A* **97**, 023824 (2018), URL <https://link.aps.org/doi/10.1103/PhysRevA.97.023824>.
  - [39] G. J. Machado, G. Frascella, J. P. Torres, and M. V. Chekhova, *Applied Physics Letters* **117**, 094002 (2020), ISSN 0003-6951, <https://pubs.aip.org/aip/apl/article-pdf/doi/10.1063/5.0016259/13914162/094002.1.online.pdf>, URL <https://doi.org/10.1063/5.0016259>.
  - [40] F. Devaux, A. Mosset, P.-A. Moreau, and E. Lantz, *Phys. Rev. X* **10**, 031031 (2020), URL <https://link.aps.org/doi/10.1103/PhysRevX.10.031031>.
  - [41] B. Ndagano, H. Defienne, D. Branford, Y. D. Shah, A. Lyons, N. Westerberg, E. M. Gauger, and D. Faccio, *Nature Photonics* **16**, 384 (2022).
  - [42] V. Giovannetti, S. Lloyd, and L. Maccone, *Nature photonics* **5**, 222 (2011).
  - [43] T. Ono, R. Okamoto, and S. Takeuchi, *Nat Commun* **4**, 2426 (2013), URL <https://www.nature.com/articles/ncomms3426#citeas>.
  - [44] Y. Israel, S. Rosen, and Y. Silberberg, *Phys. Rev. Lett.* **112**, 103604 (2014), URL <https://link.aps.org/doi/10.1103/PhysRevLett.112.103604>.
  - [45] R. Camphausen, Álvaro Cuevas, L. Duem-pelmann, R. A. Terborg, E. Wajs, S. Tisa, A. Ruggeri, I. Cusini, F. Steinlechner, and V. Pruneri, *Science Advances* **7**, eabj2155 (2021), <https://www.science.org/doi/pdf/10.1126/sciadv.abj2155>, URL <https://www.science.org/doi/abs/10.1126/sciadv.abj2155>.
  - [46] G. Brida, M. Genovese, and I. Ruo Berchera, *Nature Photonics* **4**, 227 (2010), 1004.1274.
  - [47] N. Samantaray, I. Ruo-Berchera, A. Meda, and M. Genovese, *Light: Science & Applications* **6**, e17005 EP (2017), original Article, URL <https://doi.org/10.1038/lsa.2017.5>.
  - [48] J. Sabines-Chesterking, A. R. McMillan, P. A. Moreau, S. K. Joshi, S. Knauer, E. Johnston, J. G. Rarity, and J. C. F. Matthews, *Opt. Express* **27**, 30810 (2019), URL <http://www.opticsexpress.org/abstract.cfm?URI=oe-27-21-30810>.
  - [49] I. Ruo-Berchera, A. Meda, E. Losero, A. Avella, N. Samantaray, and M. Genovese, *Applied Physics Letters* **116**, 214001 (2020), <https://doi.org/10.1063/5.0009538>, URL <https://doi.org/10.1063/5.0009538>.
  - [50] A. Monras and M. G. A. Paris, *Phys. Rev. Lett.* **98**, 160401 (2007), URL <https://link.aps.org/doi/10.1103/PhysRevLett.98.160401>.
  - [51] G. Adesso, F. Dell'Anno, S. De Siena, F. Illuminati, and L. A. M. Souza, *Phys. Rev. A* **79**, 040305 (2009), URL <https://link.aps.org/doi/10.1103/PhysRevA.79.040305>.
  - [52] R. Nair, *Phys. Rev. Lett.* **121**, 230801 (2018), URL <https://link.aps.org/doi/10.1103/PhysRevLett.121.230801>.
  - [53] E. Losero, I. Ruo-Berchera, A. Meda, A. Avella, and M. Genovese, *Scientific Reports* **8**, 7431 (2018), ISSN 2045-2322, URL <https://doi.org/10.1038/s41598-018-25501-w>.
  - [54] J. Wang, R. L. d. M. Filho, G. S. Agarwal, and L. Davidovich, *Phys. Rev. Res.* **6**, 013034 (2024), URL <https://link.aps.org/doi/10.1103/PhysRevResearch.6.013034>.
  - [55] E. Jakeman and J. Rarity, *Optics Communications* **59**, 219 (1986), ISSN 0030-4018, URL <http://www.sciencedirect.com/science/article/pii/0030401886902889>.
  - [56] G. Ortolano, A. Papiate, P. Boucher, C. Napoli, S. Soman, S. F. Pereira, I. Ruo-Berchera, and M. Genovese, *Light: Science & Applications* **12**, 171 (2023).
  - [57] M. R. Teague, *J. Opt. Soc. Am.* **73**, 1434 (1983), URL <https://opg.optica.org/abstract.cfm?URI=josa-73-11-1434>.
  - [58] D. Paganin and K. A. Nugent, *Phys. Rev. Lett.* **80**, 2586 (1998), URL <https://link.aps.org/doi/10.1103/PhysRevLett.80.2586>.
  - [59] C. Zuo, J. Li, J. Sun, Y. Fan, J. Zhang, L. Lu, R. Zhang, B. Wang, L. Huang, and Q. Chen, *Optics and Lasers in Engineering* **135**, 106187 (2020), ISSN 0143-8166, URL <https://www.sciencedirect.com/science/article/pii/S0143816619320858>.
  - [60] N. Dehghan, A. D'Errico, F. Di Colandrea, and E. Karimi, *Optica* **11**, 1115 (2024).
  - [61] P.-A. Moreau, J. Sabines-Chesterking, R. Whittaker, S. K. Joshi, P. M. Birchall, A. McMillan, J. G. Rarity, and J. C. F. Matthews, *Scientific Reports* **7**, 6256 (2017), ISSN 2045-2322, URL <https://doi.org/10.1038/s41598-017-06256-1>.

- 1038/s41598-017-06545-w.
- [62] M. Bondani, A. Allevi, G. Zambra, M. G. A. Paris, and A. Andreoni, *Phys. Rev. A* **76**, 013833 (2007), URL <https://link.aps.org/doi/10.1103/PhysRevA.76.013833>.
  - [63] G. Brida, L. Caspani, A. Gatti, M. Genovese, A. Meda, and I. R. Berchera, *Physical Review Letters* **102**, 213602 (2009).
  - [64] O. Jedrkiewicz, Y.-K. Jiang, E. Brambilla, A. Gatti, M. Bache, L. Lugiato, and P. Di Trapani, *Physical Review Letters* **93**, 243601 (2004).
  - [65] J.-L. Blanchet, F. Devaux, L. Furfaro, and E. Lantz, *Physical Review Letters* **101**, 233604 (2008).
  - [66] I. N. Agafonov, M. V. Chekhova, and G. Leuchs, *Physical Review A—Atomic, Molecular, and Optical Physics* **82**, 011801 (2010).
  - [67] A. Meda, E. Losero, N. Samantaray, F. Scafirimuto, S. Pradyumna, A. Avella, I. Ruo-Berchera, and M. Genovese, *Journal of Optics* **19**, 094002 (2017), URL <https://doi.org/10.1088/2F2040-8986/2Faa7b27>.
  - [68] D. Paganin, A. Barty, P. J. McMahon, and K. A. Nugent, *Journal of Microscopy* **214**, 51 (2004), <https://onlinelibrary.wiley.com/doi/pdf/10.1111/j.0022-2720.2004.01295.x>, URL <https://onlinelibrary.wiley.com/doi/abs/10.1111/j.0022-2720.2004.01295.x>.
  - [69] D. G. Voelz, *Computational Fourier Optics: A MATLAB Tutorial* (Spie Digital Library, 2011), ISBN 9780819482051.
  - [70] C. Zuo, Q. Chen, Y. Yu, and A. Asundi, *Optics Express* **21**, 5346 (2013).
  - [71] C. Zuo, J. Sun, J. Li, J. Zhang, A. Asundi, and Q. Chen, *Scientific Reports* **7**, 7654 (2017).